FULL PAPER

Resolving the Three-Dimensional Microstructure of Polymer Electrolyte Fuel Cell Electrodes using Nanometer-Scale X-ray Computed Tomography

William K. Epting, Jeff Gelb, and Shawn Litster*

The electrodes of a polymer electrolyte fuel cell (PEFC) are composite porous layers consisting of carbon and platinum nanoparticles and a polymer electrolyte binder. The proper composition and arrangement of these materials for fast reactant transport and high electrochemical activity is crucial to achieving high performance, long lifetimes, and low costs. Here, the microstructure of a PEFC electrode using nanometer-scale X-ray computed tomography (nano-CT) with a resolution of 50 nm is investigated. The nano-CT instrument obtains this resolution for the low-atomic-number catalyst support and binder using a combination of a Fresnel zone plate objective and Zernike phase contrast imaging. High-resolution, non-destructive imaging of the three-dimensional (3D) microstructures provides important new information on the size and form of the catalyst particle agglomerates and pore spaces. Transmission electron microscopy (TEM) and mercury intrusion porosimetry (MIP) is applied to evaluate the limits of the resolution and to verify the 3D reconstructions. The computational reconstructions and size distributions obtained with nano-CT can be used for evaluating electrode preparation, performing pore-scale simulations, and extracting effective morphological parameters for large-scale computational models.

1. Introduction

Polymer electrolyte fuel cell (PEFCs) are a promising technology to displace internal combustion engines and batteries in transportation, portable, and stationary power applications because of their high efficiencies, low device emissions, and diverse fuel supply. Much PEFC research focuses on the cathode due to the costly platinum catalyst[1] and the roughly 10% effectiveness of Pt utilization.[2,3] To decrease cost without sacrificing performance, the electrode must feature efficient oxygen and charge transport pathways through the composite microstructure. As **Figure 1**a illustrates, the electrode is composed of agglomerates of carbon-supported Pt catalyst, bound together by an ionomer, usually Nafion.[4] The carbon support particles have primary spherical diameters of roughly 40 nm, and typical Pt particle diameters are 5 nm. Smaller "primary"

pores exist within the agglomerates, while larger "secondary" pores between agglomerates support bulk oxygen and water transport.[5] Improving electrode design requires a better understanding of the electrode's morphology.

Mercury intrusion porosimetry (MIP) and gas adsorption techniques[6] have previously given valuable insight into PEFC electrode morphology[5,7–9] by measuring volumetric pore-size and surface-area distributions. However, MIP and gas adsorption are generally bulk techniques and can be limited by the effect of pore throats.[6] Transmission electron microscopy (TEM) offers high resolution and is a powerful tool for examining electrode microstructures.[8,10–16] Several minor shortcomings, discussed in Section 2.1, limit ability of using TEM to fully characterize the 3D porous structure of the electrode.[8,12,13,15,16] Two-dimensional (2D) scanning electron microscopy (SEM) can resolve carbon black particles and the larger microstructure.[8,11,13,17–20] With the additional use of destructive focused ion beam (FIB) sectioning, a series of SEM images can be computationally reconstructed into a 3D image of the electrode,[17,19,20] although it is unclear to what extent the FIB damages the ionomer.[18] Elemental mapping techniques such as back-scattered electron,[13] energy-dispersive X-ray,[11,13] and energy-filtered TEM imaging[13] as well as soft X-ray spectromicroscopy[21] can aid in imaging material distributions in electrodes.

X-ray computed tomography (XCT) offers the capability to non-destructively resolve the 3D structure of porous materials with high spatial resolution[20,22–26] using X-ray radiographs from many angles to computationally reconstruct a 3D image of the material.[6] Empty pores absorb less radiation and hence contrast with solid materials. Owing to recent developments using specialized X-ray lenses, 50 nm resolution is now available in commercial XCT equipment using Zernike phase contrast and a Fresnel zone plate objective [nanometer-scale X-ray computed tomography (nano-CT)].[22] Phase contrast is important for obtaining reasonable signal-to-noise ratios (SNR) when imaging nanometer-scale features.

In medicine and biology, nano-CT techniques have recently been used for imaging variations in bone density at

W. K. Epting, J. Gelb, Prof. S. Litster
5000 Forbes Ave, Scaife Hall 323, Pittsburgh, PA 15213, USA
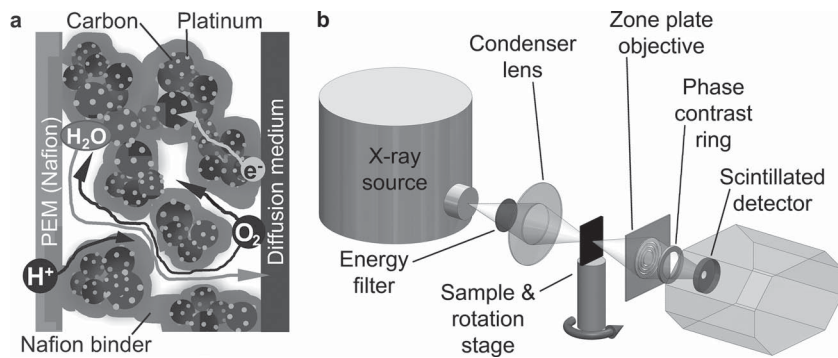E-mail: litster@andrew.cmu.edu

Figure 1. Nano-CT imaging of PEFC electrodes. a) Schematic image of a PEFC cathode that comprises agglomerates of carbon-supported Pt catalyst particles bound by a Nafion ionomer. b) Schematic image of the nano-CT instrument, which uses X-ray optics to non-destructively achieve high-resolution 3D images of both hard and soft materials. A reflective condenser optic focuses the X-rays from a laboratory X-ray source onto the sample, which rotates on a high-precision stage. The Fresnel zone plate objective is positioned past the sample. The Zernike phase ring then shifts the phase of the unscattered X-rays to enhance contrast, particularly for low-Z materials. Adapted.[22,23]

approximately 100 nm resolution[27] and visualizing metal nanoparticles in cells at 40 nm resolution.[28] In the field of electrochemistry, nano-CT has been used to investigate the morphology of solid oxide fuel cell electrodes,[22–24] where the constituent materials have high atomic numbers (Z) and high X-ray contrast. Their morphology is also very different from PEFC electrodes. In a PEFC electrode, most of the solid volume is composed of low-Z materials (carbon and fluorocarbon ionomer), although it also contains small (3–5 nm), dispersed Pt nanoparticles that occupy roughly 1% of the electrode volume. Post-mortem nano-CT has been used to obtain 2D iamges of the macroscopic Pt redistribution in a PEFC electrode to study the degradation of the electrode.[23] However, to the best of our knowledge, nano-CT has not previously been used to characterize the overall 3D structure of a PEFC electrode or of any carbon material with similar feature sizes.

In imaging PEFC electrodes, the nano-CT's 50 nm resolution does not allow to separately distinguish the individual 30–40-nm-diameter carbon support particles, the 3–5-nm-diameter platinum nanoparticles, and the 5–10-nm-thick ionomer films within the agglomerates, since these basic constituents are smaller than the resolution. Rather, nano-CT is able to provide a useful 3D characterization of the size and shape of those agglomerates, as well as the pores between them. Knowledge of the 3D structure is critical to understanding transport through the porous electrode, particularly for anisotropic materials. Additionally, because it is noninvasive and does not require a vacuum, nano-CT holds promise for in-situ imaging of PEFC electrodes. Recently, Eller et al.[25] demonstrated in operando micrometre-scale imaging of liquid water in PEFC diffusion media using XCT.

In this paper, we report our use of nano-CT to image ex situ the morphology of PEFC electrodes. The nano-CT data is used to extract volumetric distributions of the effective secondary pore and agglomerate diameters. The nano-CT measurements are validated by TEM imaging and by comparisons between MIP data and computational simulations of MIP using geometry from the nano-CT data.

2. Results and Discussion

Two PEFC electrodes were imaged using the nano-CT system (UltraXRM-L200, Xradia Inc., Pleasanton, CA) illustrated in Figure 1b. The electrodes were composed of carbon-supported Pt catalyst (Vulcan XC-72R, 20 wt% Pt/C) and a Nafion ionomer binder (35 wt% loading). The ultrasonically dispersed (10 min) catalyst ink suspension of the first electrode (Electrode 1, E1) was painted onto Kapton films rather than the typical Nafion membrane to eliminate time varying hydration and swelling of Nafion. From TEM (see the Supporting Information), the thickness of E1 was obtained as approximately 70 μm for a Pt loading of 0.9 mg Pt cm^{-2}. A second electrode sample (Electrode 2, E2) with larger agglomerates was prepared following Wilson et al.'s[29] protocol that adds tetrabutylammonium hydroxide and glycerol, and underwent only 30 s of ultrasonication.

2.1. 2D Slices and TEM Comparison

Figure 2a shows a single 2D, 32.5-nm-thick "virtual slice" from the 3D reconstruction of E1 after histogram equalization using MATLAB (Mathworks, Natick, MA). The electrode image SNR relative to the noise in adjacent open air ranged from 2.0 for E1 to 3.5 for E2 (see the Supporting Information). The higher SNR of E2 is due to the larger agglomerates and pores. In addition, fast-Fourier-transform power spectrum analysis of the nano-CT images confirmed that microstructure features of ca. 80 nm and larger were distinctly resolved (see the Supporting Information). Figure 2b shows the 2D slice after binary thresholding into solid and pore phases, with darker shades indicating the solid phase. Initially, we manually chose a threshold value by inspecting images before and after thresholding. The same value was obtained from the isodata thresholding algorithm.[30]

It is important to identify what microstructure details are lost with 50 nm nano-CT resolution since the constituent materials are smaller (e.g., ca. 40 nm diameter carbon black spheres). Figure 2c shows a higher resolution (1.72 nm pixels) TEM image of E1, cut from a different region of the nano-CT sample. Binary thresholding on this image yielded Figure 2d, showing a high level of detail that completely resolves carbon spheres. Figure 2c was then de-resolved with a Wiener filter and resized to obtain the pixel size and 50 nm resolution of the nano-CT images. Figure 2e shows the de-resolved image. Binary thresholding of Figure 2e produced Figure 2f, which qualitatively preserved the structure in Figure 2d while only losing small, isolated pores and solids. The largest inscribed pore diameter in Figure 2f was 260 nm, consistent with the larger pores in the nano-CT images of E1.

The porosity computed from this small TEM sample area was 38% in Figure 2d (before de-resolving) and 37% in Figure 2f (after de-resolving) using the same thresholding value. Based on the known thickness and composition, the porosity should be 50%. This porosity difference can occur because the ca.
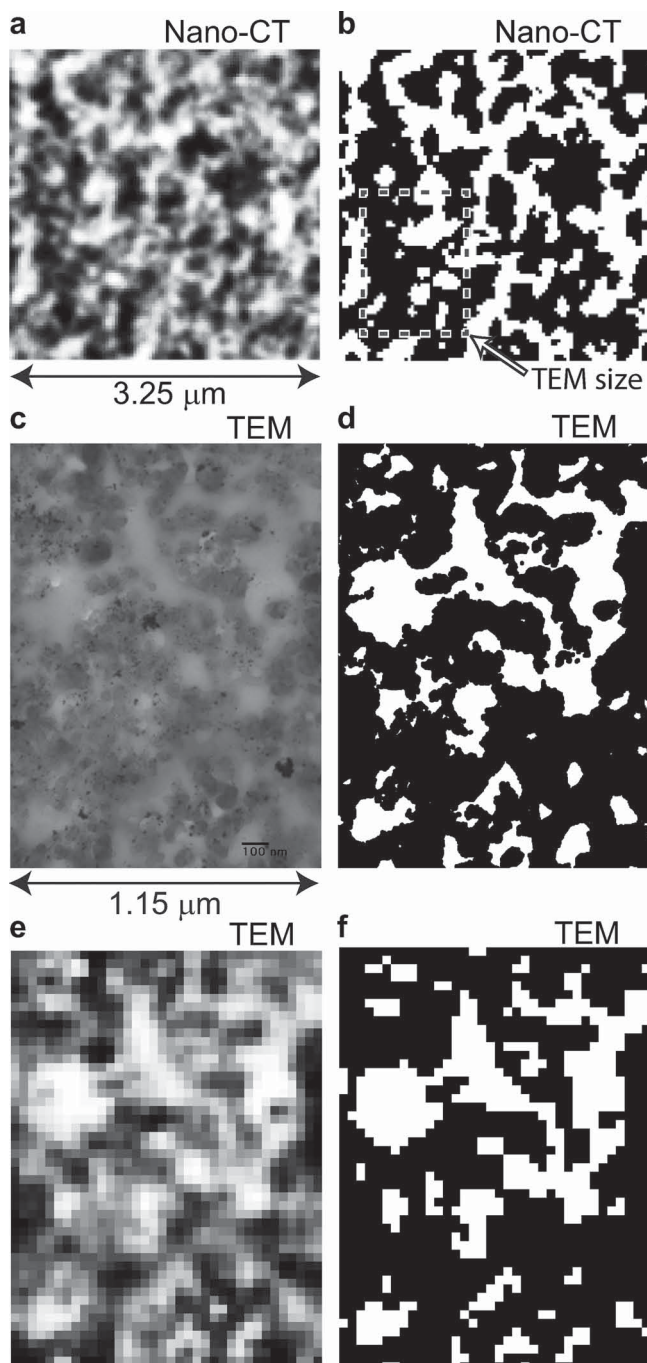
Figure 2. Verifying X-ray data with TEM images. a,b) A 2D X-ray slice of E1 before (a) and after (b) binary thresholding. The dark regions represent the solid phase in both images. c) Raw high-resolution TEM image of a separate region of E1 with 1.72 nm pixels. d) Image (c) after binary thresholding to distinguish carbon particles. e) Image (c) after filtering and resizing for a 50 nm resolution with 32.5 nm pixels. f) Image (e) after binary thresholding. Comparison between images (d) and (f) shows that the macropore structure is resolved with 50 nm resolution. Images (e) and (f) are also qualitatively similar to the X-ray CT slices in images a and b. The dashed box in image (b) depicts the relative scale of the TEM images.

100-nm-thick TEM ultramicrotome is several carbon spheres deep, which reduces apparent porosity due to simultaneous

imaging of out-of-plane carbon spheres. Another possibility is that the small TEM image is not statistically representative. We also note that agglomerate primary pores are generally difficult to resolve in TEM images.[12]

The above comparison of TEM images at different resolutions and with the nano-CT images supports that the 50 nm nano-CT resolution does not thwart characterizing the electrode's agglomerate and secondary pore structure. However, nano-CT cannot resolve the smaller primary pores within the agglomerates.[5] Also, at this time, nano-CT cannot distinguish the thin ionomer films, O(10 nm), within and around the agglomerates. From the preceding 2D and subsequent 3D analyses, it is apparent that the solid phase in nano-CT reconstructions includes the primary pore and ionomer volumes.

2.2. 3D Reconstructions

Figure 3 shows reconstructed 3D images from a cube of nano-CT data (3.25 μm side lengths) for the solid agglomerate and
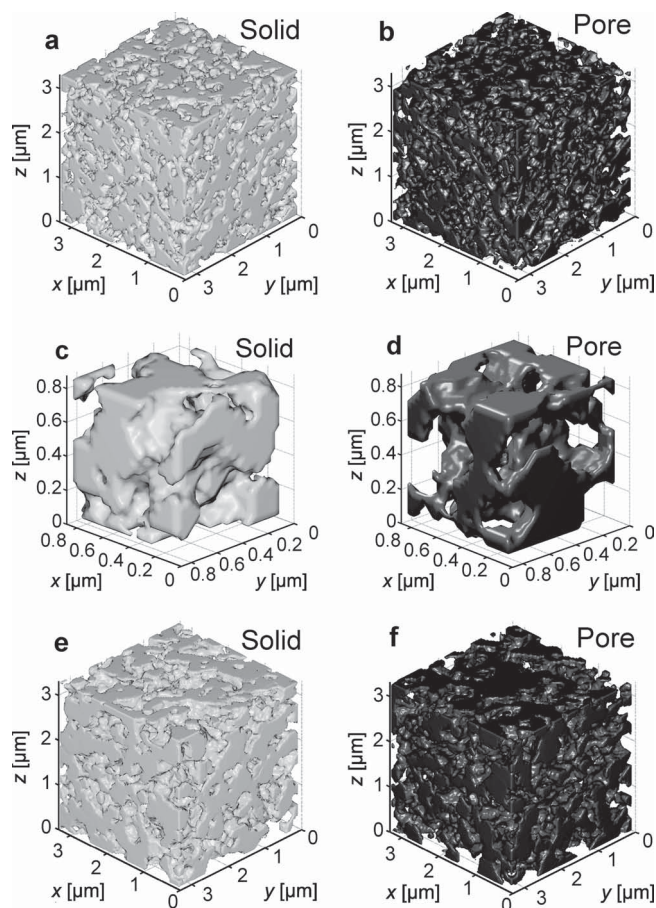

Figure 3. 3D reconstructions of PEFC electrodes. a) The 3D solid phase of E1, which includes the ionomer and primary pores. b) The 3D secondary pore phase of E1. c,d) Magnified views of the solid (c) and pore (d) phase reconstructions of E1. e,f) 3D reconstructions of solid (e) and pore (f) phases of E2. The cube dimensions in Images (a,b,e,f) are 3.25 μm × 3.25 μm × 3.25 μm. The porosity of the reconstructed E1 and E2 cubes are 43% and 41%, respectively.

pore phases of E1 and E2, including close up views for E1. This data set is valuable for future computational analysis of transport and electrochemical phenomena in PEFC electrodes. The computed porosity in the E1 and E2 cubes were 43% and 41%, respectively. The E1 value is close to, but slightly higher than, the de-resolved TEM result of 37% for E1. As described above, this may be because of the lower apparent porosity in TEM imaging and/or the small TEM image area. Indeed, a similar drop in apparent porosity was previously seen between a FIB-SEM reconstruction and a microtome image.[19] Both the nano-CT and TEM porosity values are lower than the 50% calculated from the composition and thickness. As before, this discrepancy is not surprising – the expected porosity includes the contribution of primary pores that are not considered in the TEM and nano-CT porosity values. A video in the Supporting Information shows the 3D pore phase of E1. The video exhibits the complex, tortuous transport pathways for oxygen and water through the electrode.

Figure 4. Verification of nano-CT for PEFC electrodes with MIP measurement and simulations. MIP measurement for E1 and the corresponding pore-size distributions from MIP simulations using the cubic 3D volume of Figure 3 (cube) and a thicker, non-cubic volume (thick). The relative cumulative volume is the cumulative intrusion volume divided by the total sample volume (sum of pore and solid volumes). The vertical error bars or the cube simulations are the 95% confidence internals for the six MIP simulations beginning on each face. The horizontal error bars are plus and minus half the side length of a voxel. Inset: Intrusion isosurfaces for MIP simulations for intruding spheres with diameters of 179, 146, and 114 nm in the cubic simulation, and the same for the thick simulation with 146 nm diameter spheres.

2.3. Validation with MIP

MIP was used previously to validate nano-CT results on a solid-oxide fuel cell electrode.[23] However, the omission of the throat effect in analyzing the MIP data led to poor agreement for larger pores. In our characterization of E1, the nano-CT reconstruction was verified by comparing MIP measurements with morphological MIP simulations on the nano-CT image that account for pore throat effects using an established approach.[6] The morphological MIP simulation evaluates the intrusion of spheres of decreasing diameter from a face of a 3D reconstruction to mimic the physical MIP process.

For each iteration of decreasing sphere size during the MIP simulation, the sphere diameter corresponds to an effective pore size and a certain pressure during MIP. The difference in diameter between each iteration was limited to the nano-CT's 32.5 nm voxel side length. Starting from one face of the cubic 3D reconstruction space, inscribed sphere fitting determined "seed" sites where a sphere of diameter D could intrude into the sample volume. From these seeds, inscribed spheres of the same diameter were placed in every possible inward direction. Where there was no solid phase overlap, the simulation continued to intrude spheres into adjacent unoccupied volumes. When spheres could proceed in more than one direction, a new sphere seed site and path were initialized. A sphere intrusion branch became "dead" when either a dead-end or a smaller pore throat prevented spheres from being placed in any new direction without solid overlap. After all sphere paths became dead for a given diameter, the volume corresponding to that diameter was computed and inserted to the pore-size distribution. With this simulation, the nano-CT data were made to yield pore volumes representative of those measured by MIP.

The insets of **Figure 4** show pore diameter isosurfaces at several stages of the MIP simulation as the diameter of the intruding spheres was reduced, representing the extent of mercury intrusion from a given starting face. Figure 4 presents a comparison of the simulated MIP data versus the MIP measurements. Plots are shown for two sets of simulations: 1) the mean from intrusions starting on all six faces of the largest cube
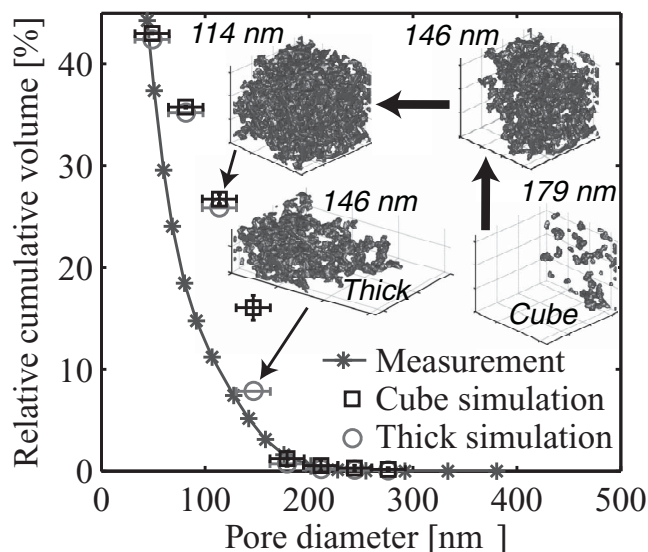
within the nano-CT data; 2) a single simulation for a thicker (6.9 μm), but non-cubic volume. The cube analysis reveals statistical variance. Since mercury does not necessarily percolate through the entire physical sample thickness at lower pressures (larger pores), the thicker nano-CT data set is more useful for comparison with MIP measurements. To compare MIP simulations with the measurements, we normalize the cumulative intruded volume by the total sample volume.

The agreement for large pores in Figure 4 is improved over that of earlier solid oxide fuel cell work.[23] For the thick simulation, all simulation data are within one voxel side length of the MIP measurement. Altogether, this analysis shows that the thresholded nano-CT data are capturing the pore-size distribution well for pore sizes greater than 50 nm. A useful insight from this analysis is the low anisotropy for MIP in this electrode based on the small vertical error bars for the six simulations on the cube.

2.4. Size Distributions

Two important outputs of this nano-CT study are the agglomerate- and pore-size distributions, which are useful for evaluating electrode designs and obtaining model inputs. **Figure 5** displays histograms of the pore- and agglomerate-size distributions based on inscribed spheres, along with related 2D slices of spatial pore- and agglomerate-size distributions. The latter
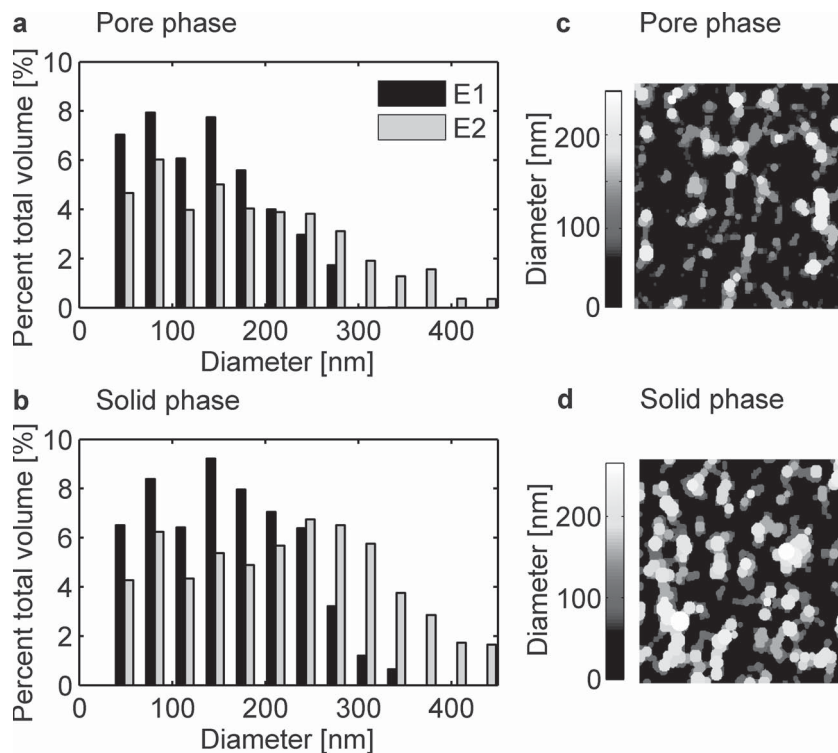
Figure 5. Pore and solid phase size distributions for PEFC electrodes. a) Solid phase size distributions for E1 and E2. The solid phase volume includes the Nafion and primary pore volumes. The peaks of the solid phase distributions are ca. 150 nm and 240 nm for E1 and E2, respectively. b) Pore-size distributions for E1 and E2. The size distributions are based on inscribed spheres and are percentages of the total volume. c,d) Spatial size distributions for the pore (c) and solid (d) phases in a 2D slice (3.25 μm × 3.25 μm) of E1 on the $z = 1.625$ μm plane, which is the same plane as Figure 2a.

show a sparse distribution of large pores within the volume. The pore-size distribution in Figure 5a captures the larger "secondary" pores well, but does not contain information regarding smaller "primary" pores that may account for roughly 5–10% of the electrode's total volume. Such a pore-size distribution can later be used for evaluating the capillary transport properties for liquid water.[31] The distribution can also be used to calculate an effective diffusion coefficient when considering Knudsen diffusion effects.[32] For example, Knudsen effects result in 65% reduction in diffusivity in a 100-nm pore.[32]

Agglomerate-size peaks can be seen in Figure 5b at ca. 150 nm and 240 nm for E1 and E2, respectively; these agree reasonably well with characteristic agglomerate sizes found by SAXS,[10] TEM,[12] and FIB-SEM.[17–20] Unlike the pore phase, the agglomerate-size distribution is not as sensitive to the 50 nm resolution, since the smallest agglomerate length scale is a carbon particle covered by ionomer film (>50 nm diameter). Several PEFC models use an effective agglomerate radius as a critical parameter in modeling the volume-average electrochemical reaction rate. However, an effective diameter from direct 3D measurements has been elusive. Using the solid agglomerate-size distribution in Figure 5b, we have calculated the volume-average agglomerate diameter to be 188 nm for E1 and 222 nm for E2 (see the Supporting Information). These diameters are much smaller than often assumed in models.[33,34]

Over-estimation of agglomerate size exaggerates the contribution of oxygen diffusion inside the agglomerates in predicting PEFC performance losses.

3. Conclusions

The present work involves an X-ray computed tomography reconstruction of two different PEFC electrode samples (E1 and E2) with a resolution of 50 nm and a cubic voxel size of 32.5 nm. De-resolved TEM images verified that the resolution of nano-CT can resolve the 3D structure of the solid and secondary pore phases in the electrode. A 3D image of an electrode reconstructed from the nano-CT data was compared with MIP and showed good agreement for pore radii significantly larger than the nano-CT resolution of 50 nm. A size peak for the solid phase was seen corresponding to characteristic diameters of ca. 150 nm and 240 nm for E1 and E2, respectively. The solid-phase size distribution gave volume-average diameters of 188 nm (E1) and 222 nm (E2) for the imaged volumes. Our analysis has demonstrated nano-CT as a technique valuable for the characterization of a PEFC electrode's 3D structure. The pore-size distributions can support the evaluation of liquid water transport and Knudsen diffusion effects during PEFC operation. The agglomerate size distributions and average diameters are valuable for evaluating the dispersion of catalyst ink suspensions and agglomerate-level mass transport effects. Furthermore, the 3D recontructions can be used for pore-scale numerical simulations. Owing to recent improvements in resolution, nano-CT now has great utility for advancing our understanding of low atomic number porous electrodes, such as those in a PEFC. In the future, nano-CT may permit in situ and even in operando electrode characterization due to its non-destructive nature and flexible sample environment.

4. Experimental Section

Sample Preparation: To prepare E1, a catalyst suspension was prepared with 20 wt% Pt/Vulcan XC-72R (Electrochem, Woburn, MA), 5 wt% Nafion DE-521 suspension (Ion Power, New Castle, DE), and de-ionized water. The Nafion was loading was 35 wt%. The mixture was agitated by a dip ultrasound mixer (Cole-Parmer, Vernon Hills, IL) for 10 min and stirred (using a magnetic stirring bar) overnight. It was then painted onto a 3 cm × 4 cm piece of 50-μm-thick Kapton HN film (DuPont, Wilmington, DE) to obviate the time-varying swelling that occurs with Nafion substrates and hinders ex situ imaging. Xie et al.[11] demonstrated that painting electrodes onto Kapton has no discernable impact on the electrode structure due to the good wettability of Kapton to catalyst suspensions. Repeated painting continued, with 30 min in a 110 °C oven between coats, until the gravimetrically determined platinum loading reached 0.9 mg cm⁻². From TEM images, the thickness

FULL PAPER

of E1 is approximately 70 μm for this Pt loading. This high loading is 2–3 times more than typical loadings and was chosen to increase the electrode volume for more accurate MIP.

The second electrode, E2, was prepared with the same volumetric composition of Pt, carbon, and Nafion as E1, but in such a way as to feature a larger pore and agglomerate diameter. This catalyst ink suspension was ion-exchanged with tetrabutylammonim hydroxide following Wilson et al.'s[29] method and featured glycerol as an additional solvent, and a shorter duration of ultrasonication (ca. 30 s).

Porosimetry and Electron Microscopy: A 3 cm × 3 cm section of the finished E1 electrode with Kapton backing was characterized by MIP to obtain pore-size distributions. The MIP was performed by Porous Materials, Inc. (Ithaca, NY). TEM samples from E1 were embedded in epoxy (EPON-Araldite, Huntsman Advanced Materials, Everburg, Belgium) for 4 days at 35 °C to prevent sample bending, and then for an additional night at 55 °C. An ultramicrotome slice was cut with a thickness of 100 nm and mounted in a Hitachi 7100 TEM. An accelerating voltage of 75 keV was used for imaging.

Nano-CT: A smaller piece (ca. 5 mm equilateral triangle) of E1 with the Kapton backing was cloven from the larger sample and placed in an UltraXRM-L200 (Xradia, Pleasanton, CA) for nano-CT (50 nm resolution, 32.5 nm cubic voxels), which uses a 8 keV laboratory X-ray source, a Fresnel zone plate objective, and Zernike phase contrast. To stabilize the thin sample in a standing position during nano-CT imaging, a triangular piece was bent with the electrode outward and the two free ends clipped together to create a loop. The radius of curvature was ca. 1 mm, which is two orders of magnitude greater than electrode thickness and thus insignificant.

Image Processing: The raw X-ray data was processed by proprietary software (Xradia, Inc.) to generate the unprocessed 3D reconstructions.[22] Subsequent analysis was performed using MATLAB (Mathworks, Natick, MA). First, the image equalization function of MATLAB was used to redistributed the raw grayscale histogram intensities over the entire intensity range to aid in visualizing the data. Then, a thresholding operation split the data into binary values representing solid (agglomerate phase) and void (pore phase). In processing TEM data, we used a similar thresholding technique to split the image into binary solid- and pore-phase data. Using the thresholded data, we characterized the solid agglomerate and pore phase size distributions based on the fitting of inscribed spheres of different diameter within the volume of each phase. The MIP simulation described in Section 2.3 was also implemented in MATLAB.

Supporting Information

Supporting Information is available from the Wiley Online Library or from the author.

Acknowledgements

[1] J. Sinha, Y. Yang, "Direct Hydrogen PEMFC Manufacturing Cost Estimation for Automotive Applications", presented at 2010 DOE Annual Merit Review, Washington, DC, **June 201**
[2] Z. T. Xia, Q. P. Wang, M. Eikerling, Z. S. Liu, *Can. J. Chem.* **2008**, *86*, 657.
[3] M. Lee, M. Uchida, H. Yano, D. A. Tryk, H. Uchida, M. Watanabe, *Electrochim. Acta* **2010**, *55*, 8504.
[4] S. Litster, G. McLean, *J. Power Sources* **2004**, *130*, 61.
[5] M. Uchida, Y. Aoyama, N. Eda, A. Ohta, *J. Electrochem. Soc.* **1995**, *142*, 4143.
[6] *Methods in the Physics of Porous Media*, (Ed: P.-Z. Wong), Academic Press, San Diego **1999**.
[7] M. Uchida, Y. Fukuoka, Y. Sugawara, N. Eda, A. Ohta, *J. Electrochem. Soc.* **1996**, *143*, 2245.
[8] J. Xie, K. L. More, T. A. Zawodzinski, W. H. Smith, *J. Electrochem. Soc.* **2004**, *151*, A1841.
[9] T. Soboleva, X. S. Zhao, K. Mallek, Z. Xie, T. Navessin, S. Holdcroft, *ACS Appl. Mater. Interfaces.* **2010**, *2*, 375.
[10] F. Xu, H. Y. Zhang, J. Ilavsky, L. Stanciu, D. Ho, M. J. Justice, H. I. Petrache, J. A. Xie, *Langmuir.* **2011**, *26*, 19199.
[11] J. Xie, F. Garzon, T. Zawodzinski, W. Smith, *J. Electrochem. Soc.* **2004**, *151*, A1084.
[12] J. Xie, D. L. Wood, K. L. More, P. Atanassov, R. L. Borup, *J. Electrochem. Soc.* **2005**, *152*, A1011.
[13] F. Scheiba, N. Benker, U. Kunz, C. Roth, H. Fuess, *J. Power Sources* **2008**, *177*, 273.
[14] Y. Shao-Horn, W. C. Sheng, S. Chen, P. J. Ferreira, E. F. Holby, D. Morgan, *Top. Catal.* **2007**, *46*, 285.
[15] C.-N. Sun, K. L. More, T. A. Zawodzinski, *ECS Trans.* **2010**, *33*, 1207.
[16] H. Uchida, J. M. Song, S. Suzuki, E. Nakazawa, N. Baba, M. Watanabe, *J. Phys. Chem. B* **2006**, *110*, 13319.
[17] C. Ziegler, S. Thiele, R. Zengerle, *J. Power Sources* **2011**, *196*, 2094.
[18] C. S. Kuroda, Y. Yamazaki, *ECS Trans.* **2007**, *11*, 509.
[19] S. Zils, M. Timpel, T. Arlt, A. Wolz, I. Manke, C. Roth, *Fuel Cells* **2010**, *10*, 966.
[20] H. Schulenburg, B. Schwanitz, J. Krbanjevic, N. Linse, R. Mokso, M. Stampanoni, A. Wokaun, G. G. Scherer, *ECS Trans.* **2010**, *33*, 1471.
[21] D. Bessarabov, A. Hitchcock, *Membrane Technol.* **2009**, *2009*, 6.
[22] A. Tkachuk, F. Duewer, H. T. Cui, M. Feser, S. Wang, W. B. Yun, *Z. Kristallogr.* **2007**, *222*, 650.
[23] S. H. Lau, et al., *J. Phys. Conf. Ser.* **2009**, *152*, 012059.
[24] P. R. Shearing, J. Gelb, J. Yi, W. K. Lee, M. Drakopolous, N. P. Brandon, *Electrochem. Commun.* **2010**, *12*, 1021.
[25] J. Eller, T. Rosen, F. Marone, M. Stampanoni, A. Wokaun, F. N. Buchi, *J. Electrochem. Soc.* **2011**, *158*, B963.
[26] A. S. Grader, A. B. S. Clark, T. Al-Dayyani, A. Nur, SCA-2009-31 in *International Symposium of the Society of Core Analysts*, Noordwijk aan Zee, The Netherlands, **September 2009**.
[27] M. Dierolf, A. Menzel, P. Thibault, P. Schneider, C. M. Kewish, R. Wepf, O. Bunk, F. Pfeiffer, *Nature* **2010**, *467*, 436.
[28] Y. S. Chu, J. M. Yi, F. De Carlo, Q. Shen, W. K. Lee, H. J. Wu, C. L. Wang, J. Y. Wang, C. J. Liu, C. H. Wang, S. R. Wu, C. C. Chien, Y. Hwu, A. Tkachuk, W. Yun, M. Feser, K. S. Liang, C. S. Yang, J. H. Je, G. Margaritondo, *Appl. Phys. Lett.* **2008**, *92*, 3.
[29] M. S. Wilson, J. A. Valerio, S. Gottesfeld, *Electrochim. Acta* **1995**, *40*, 355.
[30] T. W. Ridler, S. Calvard, *IEEETrans. Syst. Man Cybernetics* **1978**, *8*, 630.
[31] A. Z. Weber, R. M. Darling, J. Newman, *J. Electrochem. Soc.* **2004**, *151*, A1715.
[32] D. Mu, Z. S. Liu, C. Huang, N. Djilali, *Microfluid. and Nanofluid.* **2008**, *4*, 257.
[33] N. P. Siegel, M. W. Ellis, D. J. Nelson, M. R. von Spakovsky, *J. Power Sources.* **2003**, *115*, 81.
[34] W. Sun, B. A. Peppley, K. Karan, *Electrochim. Acta.* **2005**, *50*, 3359.